The Rumble in the Millimeter Wave Jungle: Obstructions Vs RIS

Juan Marcos Ramírez, Vincenzo Mancuso, Marco Ajmone Marsan
IMDEA Networks Institute, Av. Mar Mediterráneo 22, Leganés, Madrid, 28918, Spain,
Email: juan.ramirez@imdea.org, vincenzo.mancuso.imdea.org, marco.ajmone@imdea.org.

***Abstract*—Reconfigurable intelligent surfaces (RISs) have emerged as a key technology for future communication systems. RISs are arrays of tunable reflecting elements that provide controllable propagation channels by smartly shaping incident electromagnetic (EM) waves. Analysis and improvement of RIS-aided systems require the definition of accurate path loss models that consider environmental effects often encountered in practical applications. In this paper, we derive a path loss model for RIS-assisted communications to account for the attenuation induced by the transmission medium and randomly located obstructions. More precisely, this study focuses on assessing the impact caused by Poisson-located obstructing objects on RIS-assisted millimeter wave links. To this end, we evaluate the outage probability yielded by RIS-aided systems in indoor environments with antenna beam-steering and random obstructions. We obtain extensive simulation results to assess the impact of RIS considering different parameters, such as the minimum signal-to-noise ratio (SNR) necessary for successful reception, the operating frequency, the density of the Poisson process used for object placement, and the object size.**

***Index Terms*—mmWave links, path loss modeling, outage probability, reconfigurable intelligent surfaces.**

I. Introduction

Millimeter wave (mmWave) and terahertz (THz) frequency bands are expected to play a key role in the design of sixth-generation (6G) wireless communication systems. These frequency bands offer high peak data rates and broad spectra necessary to support cutting-edge applications such as immersive virtual reality, autonomous transportation systems, industrial Internet-of-things (IoT), and ultra-high-definition video streaming [1]. In contrast to sub-6 GHz channels, links operated in mmWave and THz bands exhibit severe losses when common-use objects obstruct the transmission path [2], leading to significant outage probabilities. To overcome these drawbacks, intuitive solutions include increasing the transmission power and the number of devices within the wireless network. However, these solutions also increase power consumption and infrastructure costs, making deploying these wireless systems unfeasible in various indoor environments.

In this context, reconfigurable intelligent surfaces (RIS) have recently emerged as a key supporting technology for 6G wireless communications. Specifically, these surfaces consist of arrays of reflecting elements capable of manipulating the phase and amplitude of incident electromagnetic (EM) waves, effectively reconfiguring the propagation channel [3], [4]. This technology is generally used when the line-of-sight (LOS) between the transmitter (Tx) and the receiver (Rx) is severely blocked, but a link can be established from Tx to RIS to Rx. In recent years, various free-space path loss models have been developed for the analysis and enhancement of RIS-assisted systems [5]–[11]. However, these models generally do not incorporate the effects caused by the transmission medium and the attenuation induced by objects obstructing each path associated with a RIS cell. In this scenario, developing a path loss model that considers both the characteristics of the RIS-aided channel and the attenuation caused by common-use objects is required. With the availability of a refined path loss model, it is also possible to analyze RIS-assisted systems in environments commonly encountered in practical applications using different performance criteria, including signal-to-noise ratio (SNR), spectral efficiency, and outage probability.

This work has been supported by Project AEON-CPS (TSI-063000-2021-38), funded by the Ministry of Economic Affairs and Digital Transformation and the European Union NextGeneration-EU in the Spanish Recovery, Transformation, and Resilience Plan framework.

A. Related Work

Several theoretical and experimental studies were conducted to model the path loss of RIS-assisted systems. In particular, [5] and [6] describe general path loss models that take into account the link geometry, the geometry of RIS cells, and the radiation patterns of Tx, Rx, and RIS cells. Path loss formulations for near and far fields were also developed in these works. Subsequently, [7] introduced a refined path loss model that considers more precise expressions for estimating joint radiation patterns and the relationship between scattering gain and the size of the RIS cell. Closed-form expressions for the path loss for a one-dimensional RIS-aided system can also be found in [8]. Additionally, mutual impedance-based and physics-based models were introduced in [9] and [10], respectively. Compared to the approaches mentioned above, our path loss model incorporates the effects of the attenuation of both transmission medium and obstructions on each path associated with a RIS element. Notice that our proposed path loss model is partially based on the formulation reported in [7] with major adaptations required by the consideration of the effect of obstructions. Indeed, our model considers the cumulative attenuation induced by multiple objects obstructing each of the transmission paths identified by Tx, Rx and each available RIS cell.

Different path loss models were used to evaluate the performance of wireless communication systems in terms of outage probability and SNR. In particular, [12] focused on estimating the outage probability of mmWave wireless communications, accounting for a quasi-deterministic path loss model [13] and randomly located obstructions. In addition, the work reported in [14] was aimed at estimating the probability of outages due to adversarial intervention by positioning objects that obstruct the best path. In contrast to these approaches, which only account for LOS and natural wall reflections, here we include a RIS device in the wireless system and use the proposed path loss model to estimate how the presence of the RIS can improve outage probability. The work in [15] introduced

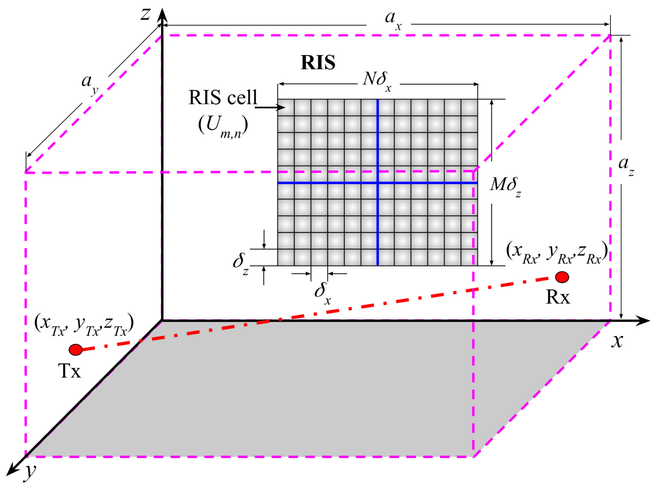

Fig. 1. Representation of the RIS-assisted wireless communication system.

a model of a RIS-aided mmWave network to estimate the SNR in indoor environments. Compared to this approach, we evaluate the proposed path loss model to estimate outage probability for RIS-assisted systems in indoor environments with randomly located objects. Based on simulation results, we also test the performance of the RIS-assisted system for different positions of the Tx and the RIS.

B. Contributions

This paper presents an improved path loss model for RIS-assisted communication systems that incorporates attenuation induced by the transmission medium and obstructions. The improved path loss model determines the outage probability of RIS-aided communication systems. Specifically, the contributions of this paper are the following:

1) We derive a refined formula to characterize the path loss of RIS-assisted wireless communication systems. This formula incorporates attenuation caused by the transmission medium and obstructions. In addition, our RIS path model also accounts for the radiation patterns of the transmitter antenna, the receiver antenna, and individual RIS cells.
2) We use the path loss model to estimate the outage probability of RIS-assisted communication systems in indoor environments with randomly located obstructions. We also show results of extensive simulations to evaluate the effect of the RIS on outage probability at mmWave frequencies (18 GHz and 60 GHz). Based on these findings, we provide insight into the design of RIS-assisted communication systems in the presence of randomly located obstructions.

C. Organization of the Paper

This paper is organized as follows. Section II describes the RIS-assisted wireless communication system that considers the attenuation induced by the transmission medium and randomly located obstructions. The behavior of the RIS-assisted system is assessed through extensive numerical simulations in Section III. Finally, Section IV summarizes some concluding remarks and future work.

II. Communication System Model

Figure 1 illustrates an indoor RIS-assisted single-input-single-output wireless communication system operating at a frequency f utilizing millimeter wave (mmWave) technology. The Cartesian coordinate system is centered at a corner of the room, with its axes aligned along the intersections of the walls. Within this spatial setup, a transmitter (Tx) and receiver (Rx) are positioned at known coordinates (x_{Tx}, y_{Tx}, z_{Tx}) and (x_{Rx}, y_{Rx}, z_{Rx}) respectively, within a walled room with length a_x, width a_y, and height a_z. In the depicted scenario, the RIS is situated on the x-z plane, with its geometric center located at (x_{Rc}, y_{Rc}, z_{Rc}). The RIS structure comprises an array of N rows and M columns of RIS cells or elements. These RIS elements have side lengths of δ_x and δ_z at subwavelength scales, typically ranging from $\lambda/10$ to $\lambda/2$, where λ denotes the wavelength of the transmitted signal.

This study focuses on estimating the outage probability of the wireless system when encountering objects randomly distributed within a walled room, potentially obstructing signal paths. Our approach involves modeling the communication channel, encompassing the LOS and RIS paths [13]. Tx and Rx are aligned using beam steering. This alignment is assumed to be optimal regarding signal-to-noise ratio (SNR), which may not correspond to the LOS path. In other words, beam steering perfectly aligns Tx and Rx with LOS or RIS paths, selecting the least attenuated path.

Considering an obstruction-filled environment, we define a two-dimensional vector $\mathcal{L} = [\mathcal{L}_0, \mathcal{L}_R]^\top$ containing the path losses in dB for the LOS and RIS paths. The path loss for the LOS path can be obtained as done in [12]:

$$\mathcal{L}_0 = L_0 + 10\log_{10}\mu_0 + \zeta X_0, \tag{1}$$

where L_0 is the free space path loss, μ_0 is a factor inversely related to the average fading depth,[1] ζ is the attenuation of the obstructing object in dB/m, which depends on the material and the operating frequency, and X_0 is the total obstruction length for the LOS path. In our model, the presence of obstructions is described by X_0, which is generally a random variable. This value refers to the distance a wave travels within one or more obstacles along the LOS path between Tx and Rx. In practical scenarios, X_0 corresponds to the length of the intersection between the linear segment connecting Tx and Rx and the obstructions encountered along this segment. In addition, the free-space path loss can be expressed as follows:

$$L_0 = 20\log_{10}(4\pi f d_0/c) - 10\log_{10}(G_t G_r) + A_0 d_0, \tag{2}$$

where d_0 represents the length of LOS path, G_t is the gain of the transmitter antenna, G_r is the gain of the receiver antenna, and A_0 stands for the transmission medium absorption loss in dB/m, which depends on the operating frequency and the composition of the transmission medium (we consider the air absorption loss).

The next step is to modify the loss model of the RIS path, reported in [6], to consider the attenuation of the transmission medium and the effects of obstructing objects.

A. The RIS Path Loss Model

In this section, we formulate an expression to estimate the path loss of a RIS link, considering the presence of randomly

[1]It should be noted that the channel coefficient is usually denoted by h/μ_0, where h represents the normalized small-scale fading. In general, h is characterized as a random variable obeying a Rayleigh statistical model such that $|h|^2$ describes an exponential distribution with a mean of one.

TABLE I

NOTATION SUMMARY AND SIMULATION PARAMETERS. NUMERICAL VALUES ARE GIVEN FOR INPUT PARAMETERS ONLY; WHEN NO VALUE IS GIVEN (INDICATED AS "-") IT IS COMPUTED DURING THE SIMULATION.

Group	Notation	Description	Input values	Unit
	Tx	Transmitter antenna	N/A	N/A
	Rx	Receiver antenna	N/A	N/A
	(x_{Tx}, y_{Tx}, z_{Tx})	Transmitter antenna coordinates	multiple positions (in 2D); (8, 3, 1) (in 3D)	m
Geometry of the scenario	(x_{Rx}, y_{Rx}, z_{Rx})	Receiver antenna coordinates	(15, 10) (in 2D); (15, 10, 2.50) (in 3D)	m
	(x_{Rc}, y_{Rc}, z_{Rc})	RIS geometric center coordinates	multiple positions (in 2D); (12, 0, 1.50) (in 3D)	m
	$U_{m,n}$	RIS cell at the m-th row and n-the column of the array	N/A	N/A
	(a_x, a_y, a_z)	Dimensions of the room	$30 \times 20 \times 3$	$\mathrm{m} \times \mathrm{m} \times \mathrm{m}$
	r_1	Distance between Tx and the center of the RIS	-	m
	r_2	Distance between the center of the RIS and Rx	-	m
	$r^t_{m,n}$	Distance between Tx and $U_{m,n}$	-	m
	$r^r_{m,n}$	Distance between $U_{m,n}$ and Rx	-	m
	d_0	Length of of the LOS path	-	m
	M	Number of rows of RIS elements	1 (in 2D); $\{8, 16\}$ (in 3D)	unitless
	N	Number of columns of RIS elements	$\{32, 64, 128, 256\}$ (in 2D); $\{8, 16\}$ (in 3D)	unitless
	(δ_x, δ_z)	Side lengths of each RIS element	$\lambda/2$	m
	$\Gamma_{m,n}$	Programmable reflection coefficient of $U_{m,n}$	-	unitless
	$B_{m,n}$	Programmable reflection coefficient amplitude of $U_{m,n}$	-	unitless
	$\phi_{m,n}$	Programmable reflection coefficient phase shift of $U_{m,n}$	-	rad
RIS	$F(\theta, \varphi)$	Normalized power radiation pattern	-	unitless
	$\theta^t_{m,n}$, $\varphi^t_{m,n}$	Elevation and azimuth angles of the path from Tx to $U_{m,n}$	-	rad
	$\theta^{m,n}_t$, $\varphi^{m,n}_t$	Elevation and azimuth angles of the path from $U_{m,n}$ to Tx	-	rad
	$\theta^{m,n}_r$, $\varphi^{m,n}_r$	Elevation and azimuth angles of the path from $U_{m,n}$ to Rx	-	rad
	$\theta^r_{m,n}$, $\varphi^r_{m,n}$	Elevation and azimuth angles of the path from Rx to $U_{m,n}$	-	rad
	$F^{(eq)}_{m,n}$	Joint normalized power normalization pattern	-	unitless
	$D^{(eq)}_{m,n}$	Joint attenuation due to medium and obstructions	-	dB
	$E^r_{m,n}$	Electric field at Rx due to $U_{m,n}$	-	V/m
	E^r	Electric field at Rx due to all RIS elements	-	V/m
	$X^t_{m,n}$	Obstruction length between Tx and $U_{m,n}$	-	m
	$X^r_{m,n}$	Obstruction length between $U_{m,n}$ and Rx	-	m
	X_0	Obstruction length for the LOS path	-	m
Obstructions	ζ	Obstruction attenuation per unit length	130 (@$f = 18$ GHz); 390 (@$f = 60$ GHz)	dB/m
	λ_{obs}	Intensity of the PPP generating the obstruction centers	[0.2, 1] (in 2D); 2 (in 3D)	m^{-2} (in 2D); m^{-3} (in 3D)
	r	Radius of the obstructing objects	< 0.5	m
	c	Speed of light through the air	299 792 458	m/s
	f	Operating mmWave frequency	$\{18, 60\}$	GHz
Antennas and propagation	λ	Signal wavelength	$\frac{c}{f}$	m
	Z_0	Impedance characteristic of the air	376.73	Ω
	G_t	Gain of the transmitter antenna	20	dB
	G_r	Gain of the receiver antenna	10	dB
	A_r	Aperture of the receiver antenna	$\frac{Gr\lambda^2}{4\pi}$	m^2
	P_t	Power transmitted by Tx	0.1	W
	P^{Rx}_r	Power received at Rx	-	W
	$P_{n,m}$	Power received by $U_{m,n}$	-	W
	μ_0	Fading scale factor for the LOS path	1	unitless
	A_0	Absorption loss of the transmission medium (air)	0.00006 (@$f = 18$ GHz); 0.0015 (@$f = 60$ GHz)	dB/m
Link budget	L_0	Free space path loss for the LOS path	-	dB
	$\mathcal{L}_0$	Path loss for the LOS path	-	dB
	$\mathcal{L}_R$	Path loss for the RIS path	-	dB
	σ^2	AWGN noise variance	$1.65 \cdot 10^{-11}$	W
	γ_k	SNR of the k-th path after antenna beamsteering	-	unitless
	Υ	Loss of the least attenuated path	-	dB
	$\mathrm{P_{out}}$	Outage probability	-	unitless

positioned obstacles and the attenuation characteristics of the transmission medium. To achieve this, we take into account the RIS-assisted communication system model reported in [6] to obtain an expression for the RIS path loss. More precisely, our study examines RIS-assisted communication systems in the near-field[2]. In this regard, let us define $U_{m,n}$ as the RIS cell situated at the m-th row and n-th column within the array, characterized by a reconfigurable reflection coefficient denoted as $\Gamma_{m,n} = B_{m,n}e^{-j\phi_{m,n}}$, where $B_{m,n}$ and $\phi_{m,n}$ represent the programmable amplitude and phase shift of the RIS element $U_{m,n}$, respectively. For the configuration depicted in Figure 1, the geometric center of $U_{m,n}$ is positioned at coordinates $\left((n-\frac{1}{2})\delta_x + x_{Rc}, 0, (m-\frac{1}{2})\delta_z + z_{Rc}\right)$, where n and m are integer numbers: $n \in \{1-\frac{N}{2}, 2-\frac{N}{2}, \ldots, \frac{N}{2}\}$ and $m \in \{1-\frac{M}{2}, 2-\frac{M}{2}, \ldots, \frac{M}{2}\}$, with N and M even. Moreover, let us consider r_1, r_2, $r^t_{m,n}$, and $r^r_{m,n}$ as follows: r_1 represents the distance between Tx and the center of the RIS, r_2 denotes the distance between the center of the RIS and Rx, $r^t_{m,n}$ is the distance between Tx and the center of $U_{m,n}$, and $r^r_{m,n}$ denotes the distance between the center of $U_{m,n}$ and Rx. Within this framework, considering the presence of obstructive objects and the attenuation effects of the transmission medium, the power received by the element $U_{m,n}$ from the transmitter $P_{m,n}$ can be expressed as follows:

$$P_{m,n} = \frac{P_t G_t F(\theta^t_{m,n}, \varphi^t_{m,n}) F(\theta^{m,n}_t, \varphi^{m,n}_t)\delta_x\delta_z}{4\pi \left(r^t_{m,n}\right)^2 10^{\frac{A_0 r^t_{m,n}}{10}} 10^{\frac{\varsigma X^t_{m,n}}{10}}}, \quad (3)$$

where P_t is the power transmitted by Tx, $F(\theta^t_{m,n}, \varphi^t_{m,n})$ is the normalized power radiation pattern of the transmitter antenna, $F(\theta^{m,n}_t, \varphi^{m,n}_t)$ is the normalized power radiation pattern of $U_{m,n}$. The normalized power radiation pattern refers to the variation of the power radiated or received by an antenna, based on the direction in which the maximum power is transmitted or received. In the spherical coordinate system, this variation is as function $F(\theta, \varphi)$ given by

$$F(\theta,\varphi) = \begin{cases} \cos^\alpha \theta & \theta \in \left[0, \frac{\pi}{2}\right], \varphi \in [0, 2\pi] \\ 0 & \theta \in \left[\frac{\pi}{2}, \pi\right], \varphi \in [0, 2\pi] \end{cases}, \quad (4)$$

where θ and φ represent elevation and azimuth angles relative to the direction of maximum transmission and reception power.

In our approach, $\theta^t_{m,n}$ and $\varphi^t_{m,n}$ denote the elevation and azimuth angles characterizing the path from Tx to the center of the RIS cell $U_{m,n}$. This characterization considers the path between Tx and the center of the RIS as the direction of maximum power transmission. For $F(\theta^t_{m,n}, \varphi^t_{m,n})$, $\alpha = \frac{G_t}{2} - 1$, where G_t is the gain of the transmitter antenna. On the other hand, $\theta^{m,n}_t$ and $\varphi^{m,n}_t$ represent the elevation and azimuth angles corresponding to the link from the center of $U_{m,n}$ to Tx. Here, we consider the vector orthogonal to $U_{m,n}$ as the direction of maximum power reception. For the expression of $F(\theta^{m,n}_t, \varphi^{m,n}_t)$, we use $\alpha = 1$ due to the simplicity of the shape of each single RIS cell.

[2]There are differences between the near field and the far field depending on the distance between the transmitter and the center of the RIS. Specifically, the near field is considered when the distance from the terminal (Tx or Rx) to the RIS center is between 5λ and $\frac{2D^2}{\lambda}$, where D is the RIS array side size. For an operating frequency of 18 GHz, $\delta_x = \delta_z = \frac{\lambda}{2}$, and 64 RIS elements, the near field boundaries are 83.33 mm and 68.22 m. In addition, for 60 GHz, $\delta_x = \delta_z = \frac{\lambda}{2}$, and 64 RIS elements, the near field boundaries are 24.98 mm and 20.47 m.

Note that in (3) the term $10^{\frac{A_0 r^t_{m,n}}{10}} 10^{\frac{\varsigma X^t_{m,n}}{10}}$ includes attenuation induced by the transmission medium and randomly located obstructions. In this context, $X^t_{m,n}$ represents the length obstructing the path between Tx and $U_{m,n}$. As previously discussed regarding X_0 in the LOS path loss model, $X^t_{m,n}$ represents the (random) intersection between the line segment extending from Tx to the center of RIS cell $U_{m,n}$ and the randomly positioned obstructions. Observe that the quantity of obstructed paths between the transmitter and all RIS elements, the number of obstacles blocking each path between the transmitter and each RIS element, and the length of each intersection are all random variables. This adds significant complexity to modeling both the path loss and the outage probability, particularly in the near-field. Furthermore, the possibility of a single obstacle obstructing various paths between Tx and RIS further complicates the modeling process.

Subsequently, the power reflected by the RIS element $U_{m,n}$ is expressed as $P'_{n,m} = P_{m,n}|\Gamma_{n,m}|^2$, where $\Gamma_{m,n}$ denotes the reflection coefficient of $U_{m,n}$, defined as $\Gamma_{m,n} = B_{m,n}e^{-j\phi_{m,n}}$ [6]. Following this reflection, the received power at Rx from $U_{m,n}$ is given by:

$$P^r_{m,n} = \frac{P'_{m,n} F(\theta^{m,n}_r, \varphi^{m,n}_r) F(\theta^r_{m,n}, \varphi^r_{m,n}) A_r}{4\pi \left(r^r_{m,n}\right)^2 10^{\frac{A_0 r^r_{m,n}}{10}} 10^{\frac{\varsigma X^r_{m,n}}{10}}} \quad (5)$$

where $\theta^{m,n}_r$ and $\varphi^{m,n}_r$ stand for the elevation and azimuth angles of the path from the center of $U_{m,n}$ to Rx, considering the vector orthogonal to $U_{m,n}$ as the direction of maximum power transmission. For reflections from a RIS cell towards Rx, being the cell very simple in shape, we use $\varphi^{m,n}_r)$, $\alpha = 1$ in the expression of $F(\theta^{m,n}_r$. Moreover, $\theta^r_{m,n}$ and $\varphi^r_{m,n}$ denote the elevation and azimuth angles of the path from Rx to $U_{m,n}$, considering the path between Rx and the RIS center as the direction of maximum power reception, and the normalized power radiation pattern is indicated as $F(\theta^r_{m,n}, \varphi^r_{m,n})$, in which we use $\alpha = \frac{G_r}{2} - 1$, where G_r is the gain of the receiving antenna. Additionally, A_r is the aperture of the receiving antenna, and $X^r_{m,n}$ is the obstruction length for the path between $U_{m,n}$ and Rx. $X^r_{m,n}$ is a random variable that we evaluate in the same way as $X^t_{m,n}$ and X_0. Substituting the reflected power $P'_{m,n}$ and (3) in (5), we have

$$P^r_{m,n} = \frac{P_t G_t F^{(eq)}_{m,n} \delta_x \delta_z A_r |\Gamma_{m,n}|^2}{16\pi^2 \left(r^t_{m,n}\right)^2 \left(r^r_{m,n}\right)^2 D^{(eq)}_{m,n}}, \quad (6)$$

where $F^{(eq)}_{m,n}$ is the joint normalized power radiation pattern that can be expressed as [7]:

$$\begin{aligned} F^{(eq)}_{m,n} &= F(\theta^t_{m,n}, \varphi^t_{m,n}) F(\theta^{m,n}_t, \varphi^{m,n}_t) \\ &\quad \cdots \times F(\theta^{m,n}_r, \varphi^{m,n}_r) F(\theta^r_{m,n}, \varphi^r_{m,n}) \quad (7) \\ &= \cos(\theta^t_{m,n})^{\left(\frac{G_t}{2}-1\right)} \cos(\theta^{m,n}_t) \cos(\theta^{m,n}_r) \\ &\quad \cdots \times \cos(\theta^r_{m,n})^{\left(\frac{G_r}{2}-1\right)}, \quad (8) \end{aligned}$$

and $D^{(eq)}_{m,n}$ is the joint attenuation due to the transmission medium and the randomly located obstructions, which can be described as:

$$D^{(eq)}_{m,n} = 10^{\frac{A_0\left(r^t_{m,n} + r^r_{m,n}\right)}{10}} 10^{\frac{\varsigma\left(X^t_{m,n} + X^r_{m,n}\right)}{10}}. \quad (9)$$

Observe that the joint attenuation described in (9) considers the attenuation between Tx and each element of the RIS

$U_{m,m}$, and the attenuation between $U_{m,n}$ and Rx. The electric field at Rx due to the RIS element $U_{m,n}$ can be written as follows:

$$E^r_{m,n} = \sqrt{\frac{2Z_0 P^r_{m,n}}{A_r}} e^{-j\frac{2\pi\left(r^t_{m,n}+r^r_{m,n}\right)}{\lambda}} = \sqrt{\frac{Z_0 P_t G_t F^{(eq)}_{m,n}\delta_x\delta_z}{8\pi^2 D^{(eq)}_{m,n}}} \frac{\Gamma_{m,n} e^{-j\frac{2\pi\left(r^t_{m,n}+r^r_{m,n}\right)}{\lambda}}}{r^t_{m,n} r^r_{m,n}}, \quad (10)$$

where Z_0 is the air characteristic impedance. In terms of all RIS elements, the electric field received at Rx can be expressed as $\sum_{m=1}^{M}\sum_{n=1}^{N} E^r_{m,n}$ [6], i.e.:

$$E^r = \sqrt{\frac{Z_0 P_t G_t \delta_x \delta_z}{8\pi^2}} \times \sum_{m=1}^{M}\sum_{n=1}^{N} \sqrt{\frac{F^{(eq)}_{m,n}}{D^{(eq)}_{m,n}}} \frac{\Gamma_{m,n} e^{-j\frac{2\pi\left(r^t_{m,n}+r^r_{m,n}\right)}{\lambda}}}{r^t_{m,n} r^r_{m,n}}. \quad (11)$$

The power received at Rx in terms of all elements of the RIS is defined as $P_r^{Rx} = (A_r|E^r|^2)/(2Z_0)$ [6], where the aperture of the antenna at the receiver is given by $A_r = (G_r\lambda^2)/(4\pi)$. Therefore, the power received at Rx can be expressed as:

$$P_r^{Rx} = \frac{P_t G_t G_r \delta_x \delta_z \lambda^2}{64\pi^3} \times \left| \sum_{m=1}^{M}\sum_{n=1}^{N} \sqrt{\frac{F^{(eq)}_{m,n}}{D^{(eq)}_{m,n}}} \frac{\Gamma_{m,n} e^{-j\frac{2\pi\left(r^t_{m,n}+r^r_{m,n}\right)}{\lambda}}}{r^t_{m,n} r^r_{m,n}} \right|^2. \quad (12)$$

Assuming that all the reflection coefficients have the same amplitude B and different programmable phase shifts $\phi_{m,n}$, the power received at Rx can be rewritten as:

$$P_r^{Rx} = \frac{P_t G_t G_r \delta_x \delta_z \lambda^2 B}{64\pi^3} \times \left| \sum_{m=1}^{M}\sum_{n=1}^{N} \sqrt{\frac{F^{(eq)}_{m,n}}{D^{(eq)}_{m,n}}} \frac{e^{-j\frac{2\pi\left(r^t_{m,n}+r^r_{m,n}\right)}{\lambda}+j\phi_{m,n}}}{r^t_{m,n} r^r_{m,n}} \right|^2, \quad (13)$$

whose maximum value for the desired coordinates of Rx is given by

$$P_r^{Rx} = \frac{P_t G_t G_r \delta_x \delta_z \lambda^2 B}{64\pi^3} \left| \sum_{m=1}^{M}\sum_{n=1}^{N} \sqrt{\frac{F^{(eq)}_{m,n}}{D^{(eq)}_{m,n}}} \frac{1}{r^t_{m,n} r^r_{m,n}} \right|^2, \quad (14)$$

which is reached when

$$\phi_{m,n} = \mod\left(\frac{2\pi\left(r^t_{m,n}+r^r_{m,n}\right)}{\lambda}, 2\pi\right). \quad (15)$$

In this work, we assume that phase shifts $\phi_{m,n}$ are designed so that each RIS element's reflected signal steers to the desired coordinates of Rx. Therefore, the loss of the RIS path can be expressed, in dB, as:

$$\mathcal{L}_R = 10\log_{10}\left(\frac{64\pi^3}{G_t G_r \delta_x \delta_z \lambda^2 B} \frac{1}{\left| \sum_m \sum_n \sqrt{\frac{F^{(eq)}_{m,n}}{D^{(eq)}_{m,n}}} \frac{1}{r^t_{m,n} r^r_{m,n}} \right|^2} \right). \quad (16)$$

Finally, we can obtain a refined version of the path loss for the RIS by considering the relationship between the scattering gain and the size of the RIS element reported in [7], i.e., the argument of the logarithmic function in (16) is multiplied by $\lambda^2/(4\pi\delta^2)$, which generates

$$\mathcal{L}_R = 20\log_{10}\left(\frac{4\pi}{\delta_x\delta_z}\right) - 10\log_{10}(G_t G_r B) - 20\log_{10}\left| \sum_{m=1}^{M}\sum_{n=1}^{N} \sqrt{\frac{F^{(eq)}_{m,n}}{D^{(eq)}_{m,n}}} \frac{1}{r^t_{m,n} r^r_{m,n}} \right|. \quad (17)$$

In the above equation, the path loss on the RIS pathway is determined by the attenuations along all paths extending from the transmitter to all elements of the RIS, as well as the attenuations along the paths from the cells of the RIS to Rx.

B. SNR and outage probability

Once the path loss model for RIS-assisted systems has been defined, and assuming that additive noise entries are modeled as independent and identically distributed (iid) random samples following a zero-mean Gaussian distribution with variance σ^2, and the squared channel fading $|h|^2$ as a random observation obeying an exponential distribution with mean one, the signal-to-noise ratio (SNR) after beam-steering aligns antennas at path k can be expressed as

$$\gamma_k = \frac{P_t|h|^2}{\sigma^2} 10^{-\frac{\mathcal{L}_k}{10}}. \quad (18)$$

Additionally, assuming that the beam steering of antennas is optimal for each path, the SNR corresponds to the path selected using beam steering. In practice, this means that Tx samples the LOS and the other available paths and selects the one that shows the least (observed) average attenuation; in other words

$$\gamma = \frac{P_t|h|^2}{\sigma^2\Upsilon}, \quad (19)$$

where the denominator models the effects of using beam-steering to select the least attenuated path, through Υ:

$$\Upsilon = \min_k \left\{10^{\frac{\mathcal{L}_k}{10}}\right\}. \quad (20)$$

For simplicity, we assume that if Tx chooses to steer its beam towards the RIS, it will align the beam with the center of the RIS. If the RIS is selected, the phase shift of each RIS cell's reflection coefficient will be adjusted to ensure that the RIS directs the maximum power directly towards the coordinates of Rx.

The outage probability is the probability that the SNR be below a decoding threshold γ_{th} (or below a threshold for which the error rate of the decoder be acceptable). Hence, the outage probability is defined as

$$\mathrm{P}_{\text{out}}(\gamma_{\text{th}}) = \Pr(\Upsilon \le \gamma_{\text{th}}). \quad (21)$$

III. NUMERICAL SIMULATIONS

This section presents the outcomes of extensive numerical simulations to assess the outage probability of RIS-assisted systems in the presence of randomly positioned obstructions. To achieve this objective, we adopt the derived path loss model that considers both the attenuation of the transmission medium and obstructions on wireless links. Initially, we show the results for a 2D indoor setting, exploring various configurations of the RIS-aided system. Subsequently, we

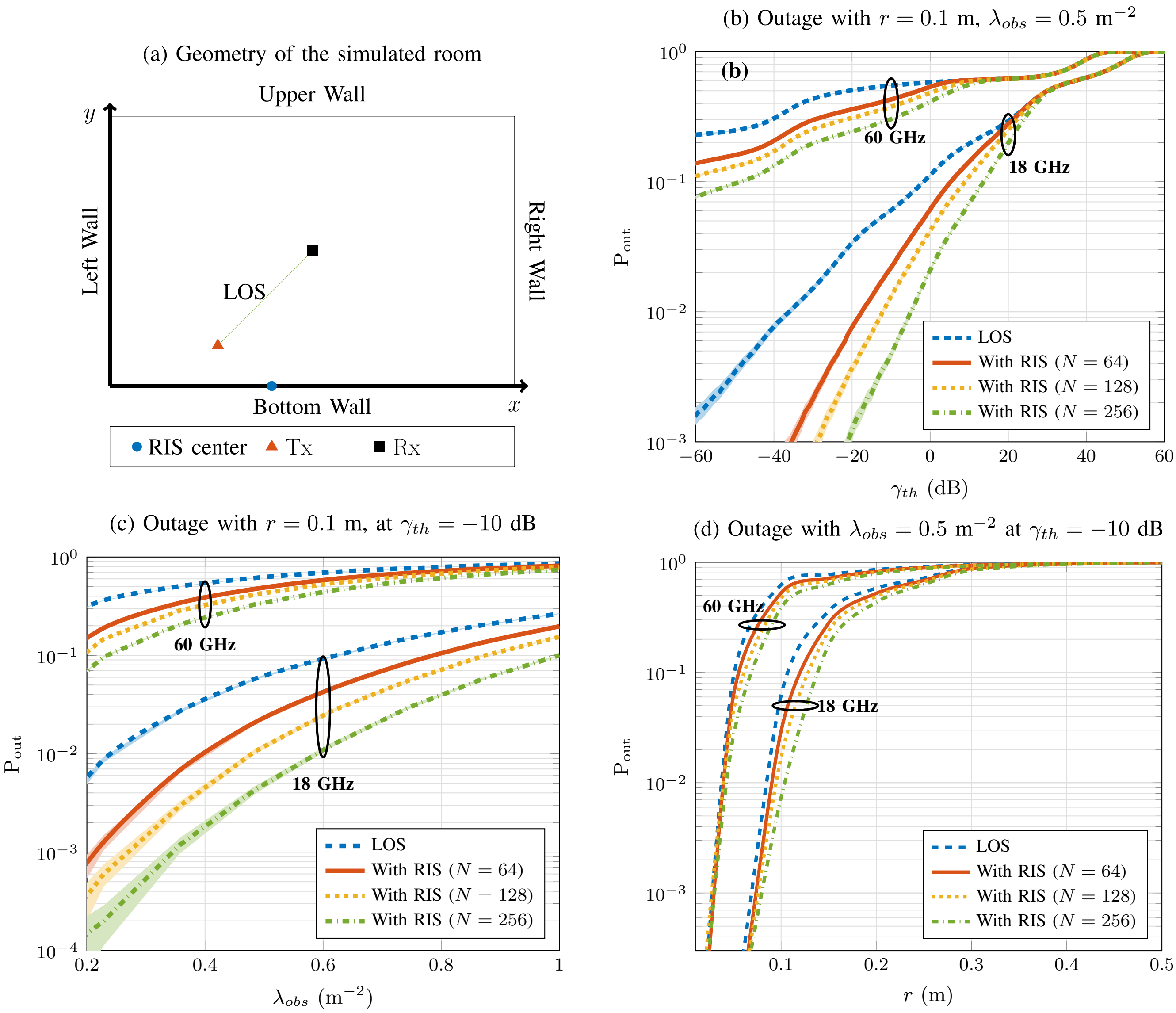

Fig. 2. (a) Simulated Indoor 2D geometry: positions Tx : $(8, 3)$, Rx : $(15, 10)$, and RIS center at $(12, 0)$. Outage probability (P_{out}) with 95% confidence interval (b) as a function of SNR threshold (γ_{th}) for the direct LOS path (LOS) and the system considering the LOS and RIS paths (With RIS) using different numbers of RIS elements N; (c) versus the density of the PPP process λ_{obs} for different numbers of RIS elements N at $\gamma_{th} = -10$ dB; and (d) versus obstruction radius r for different N values and $\gamma_{th} = -10$ dB.

analyze the performance of RIS-assisted wireless links across different beam steering scenarios. Finally, we examine a 3D indoor scenario under a specific system setup.

The various configurations of the RIS-assisted wireless system were implemented in Python using the Numpy library [3]. In addition, simulations were conducted on a Dell Inspiron 14 7000 laptop with an 11th Gen Intel Core i7 CPU operating at 2.80 GHz and 32 GB of RAM. Notably, each point in our results was derived from averaging $100,000$ realizations of the respective experiment. At each trial, the simulation generates a new Poisson point process (PPP) realization for randomly positioning the centers of obstructing objects. It is pertinent to mention that the estimation of every outage probability curve takes approximately five minutes.

A. Indoor 2D

This section provides simulation results for the two-dimensional (2D) indoor scenario. Here, for simplicity, we focus on a planar scenario where the transmitter, the receiver, and the RIS are situated on a plane parallel to the ground. Moreover, we assume $N > 1$ and $M = 1$ for the RIS configuration, representing a linear RIS comprising N cells of size δ_x^2 arranged on the selected plane, and we can restrict simulations to that plane only. Consequently, obstructions here are simulated as circles of radius r.

Specifically, we have simulated a rectangular room with dimensions of 20 m width and 30 m length. These dimensions represent realistic indoor environments, including office spaces, classrooms, conference rooms, meeting rooms, and halls. We account for objects and humans within the room, which may obstruct wireless communication links [16]. As illustrated in Fig. 2(a), the origin of the Cartesian coordinate system is located at the bottom-left corner of the room, and the two axes of the coordinate system are aligned with the left and bottom walls. The mmWave transmitter and receiver are at coordinates Tx: $(8, 3)$ and Rx: $(15, 10)$, respectively. Therefore, the distance between the transmitter and receiver is $d_0 = 9.90$ m. In this scenario, the RIS is aligned with

[3]The source code of the simulations can be downloaded from this link: https://github.com/JuanMarcosRamirez/outage_RIS_indoor

the bottom wall of the room, and its geometric center is at coordinates: $(12, 0)$. The common amplitude of the RIS cell reflection coefficient is fixed at $B = 1$.

For our numerical study, we have set the side length of the RIS cell to $\delta_x = \frac{\lambda}{2}$ with $\delta_x = 8.33$ mm for 18 GHz and $\delta_x = 2.50$ mm for 60 GHz. In the indoor 2D case context, we evaluate the performance of the RIS-assisted wireless system using RIS arrays with $N = 32$, $N = 64$, and $N = 128$ cells. This work sets the inter-cell distance as the cell side size, i.e., $\frac{\lambda}{2}$, so no space exists between RIS elements. Consequently, the RIS array widths along the x-coordinate for 18 GHz are $N\delta_x = 0.53$ m, $N\delta_x = 1.07$ m, $N\delta_x = 2.13$ m, for $N = 64$, $N = 128$, and $N = 256$, respectively. Similarly, for 60 GHz, the RIS widths along the x-coordinate are $N\delta_x = 0.16$ m, $N\delta_x = 0.32$ m, $N\delta_x = 0.64$ m, for $N = 64$, $N = 128$, and $N = 256$, respectively. In the simulation settings, we have set the intensity of the obstruction PPP to $\lambda_{obs} = 0.5$, except for the experiments that evaluate the outage probability as a function of λ_{obs}. In addition, we have used a radius of $r = 10$ cm for all experiments except for those that determine the outage probability based on the radius of obstructing objects. Additionally, we set the fading factor to $\mu_0 = 1$ and fix the gains of transmitter and receiver antennas at G_t = 20 dB and G_r = 10 dB, respectively. The transmission power is set to $P_t = 0.1$ W, and the AWGN noise variance is fixed to $\sigma^2 = 1.65 \times 10^{-11}$ W. Finally, Table I displays the values of air absorption attenuation A_0 and obstruction attenuation ζ for 18 GHz and 60 GHz.

This study generates a random number of objects at every trial, and their centers are positioned randomly according to a PPP with intensity λ_{obs}. Subsequently, the path between Tx and Rx is defined for the LOS path, and the distances between the object centers and the LOS path are calculated. If the distance between the LOS path and an obstructing object is less than r, the obstruction length X_0^k is computed as $X_0^k = 2r\cos(\arcsin(\frac{\ell_k}{r}))$, where ℓ_k is the orthogonal distance between the LOS path and the object center. If multiple objects obstruct the LOS path, we obtain the obstruction length for the LOS path as $X_0 = \sum_{k=0}^{\kappa} X_0^k$, where κ is the number of objects obstructing the LOS path. Then, the path loss of the LOS path $\mathcal{L}_0$ is computed using (1). Similarly, the simulation calculates the length obstructing the path between Tx and the RIS cell $U_{m,n}$ (or between Rx and the RIS cell $U_{m,n}$), resulting in $X_{m,n}^t$ (or $X_{m,n}^r$). The obstruction length is determined for all RIS elements, and the path loss of the RIS path $\mathcal{L}_R$ is computed using (17)

Fig. 2(b) presents simulation results, accompanied by 95% confidence intervals, illustrating the outage probability plotted against the threshold γ_{th} for varying numbers of RIS elements ($N = 64$, $N = 128$, $N = 256$). These curves are generated for two distinct operating frequencies, specifically $f = 18$ GHz and $f = 60$ GHz. Additionally, the figure illustrates the outage probability exclusively when utilizing the LOS path.

Incorporating the RIS yields a notable enhancement in the performance of the wireless communication system in contrast to relying solely on the LOS path. For instance, when maintaining the outage probability at 0.1% ($\mathrm{P_{out}} = 0.001$) and operating at a frequency of 18 GHz, the improvement achieved by the RIS-assisted system over a pure LOS setup amounts to approximately 30 dB, 38 dB, and 45 dB for $N = 64$, $N = 128$, and $N = 256$, respectively. Hence, a substantial enhancement in system performance is achievable with an increasing number of RIS elements. It is also observed that outage probabilities are higher at 60 GHz than at 18 GHz, but usable SNR thresholds show a notable gain due to an increase in the horizontal shift of the curves. This behavior at higher frequencies is attributed to the significant increase of the object attenuation coefficient ζ and the reduced size of RIS elements, both associated with higher frequencies. In addition, it is noteworthy that the impact of air absorption on system performance is minimal.

Fig. 2(c) illustrates the influence of the density of the PPP λ_{obs} across different numbers of RIS elements. For these curves, we set the SNR threshold to $\gamma_{th} = -10$ dB, maintaining the positions of the RIS center, transmitter, and receiver consistent with those in Fig. 2(a). As expected, the figure shows higher outage probabilities as λ_{obs} increases. In addition, the substantial benefits introduced by the RIS persist across all scenarios. Furthermore, the figure indicates that employing beam-steering to select the path with the least attenuation yields improved performance as the number of RIS elements grows. To conclude the study of performance with fixed positions, Fig. 2(d) shows how the obstruction radius r affects the outage probability in that scenario, at $\gamma_{th} = -10$ dB. The figure shows that outage probabilities increase rapidly as the obstruction radius increases. Moreover, the number of RIS cells has a negligible effect on outage probabilities.

Next, we show outage probability results for different RIS positions and locations of Tx, with Rx positioned at the center of the room. Specifically, Fig. 3(a) illustrates the test positions utilized for RIS centers and Tx locations, while the coordinates of Rx are denoted as (15, 10) in meters. For each RIS location, we estimate the $\mathrm{P_{out}}$ curve for all positions of the Tx. In addition, Tx positions are uniformly spaced one meter apart horizontally or vertically, while RIS centers are spaced two meters apart along the room perimeter.

Fig. 3(b) displays a heatmap indicating the outage probability of the RIS-assisted wireless system across all Tx positions and all positions of the RIS center, as depicted in Figure 3(a). More precisely, the heatmap is obtained for an SNR threshold $\gamma_{th} = -10$ dB, with $N = 128$ RIS elements and an operating frequency of $f = 18$ GHz. For each Tx position, we compute the average outage probability considering all possible locations of the RIS center. For comparison purposes, Fig. 3(c) depicts a heatmap containing the outage probability of the wireless system without RIS across all Tx positions. The performance enhancement of the RIS-assisted system in terms of outage probability with respect to the case without RIS is evident in the regions near the room perimeter. However, this enhancement extends across the entire room. To quantify this impact, Figure 3(d) illustrates the relative gain (g_{RIS}) for each transmitter Tx position, considering an SNR threshold of $\gamma_{th} = -10$ dB, with $N = 128$ cells, and a frequency of $f = 18$ GHz. More precisely, the relative gain is computed as follows:

$$g_{\mathrm{RIS}} = \frac{\mathrm{P_{out}^{[No\ RIS]}} - \mathrm{P_{out}^{[With\ RIS]}}}{\mathrm{P_{out}^{[No\ RIS]}}} . \tag{22}$$

The value of g_{RIS} captures the gain of incorporating a RIS in the wireless systems. Specifically, the heatmap of Fig. 3(d) shows that RIS enables an average gain of over 25% in a significant portion of the room. Figs 3(e)-(f)

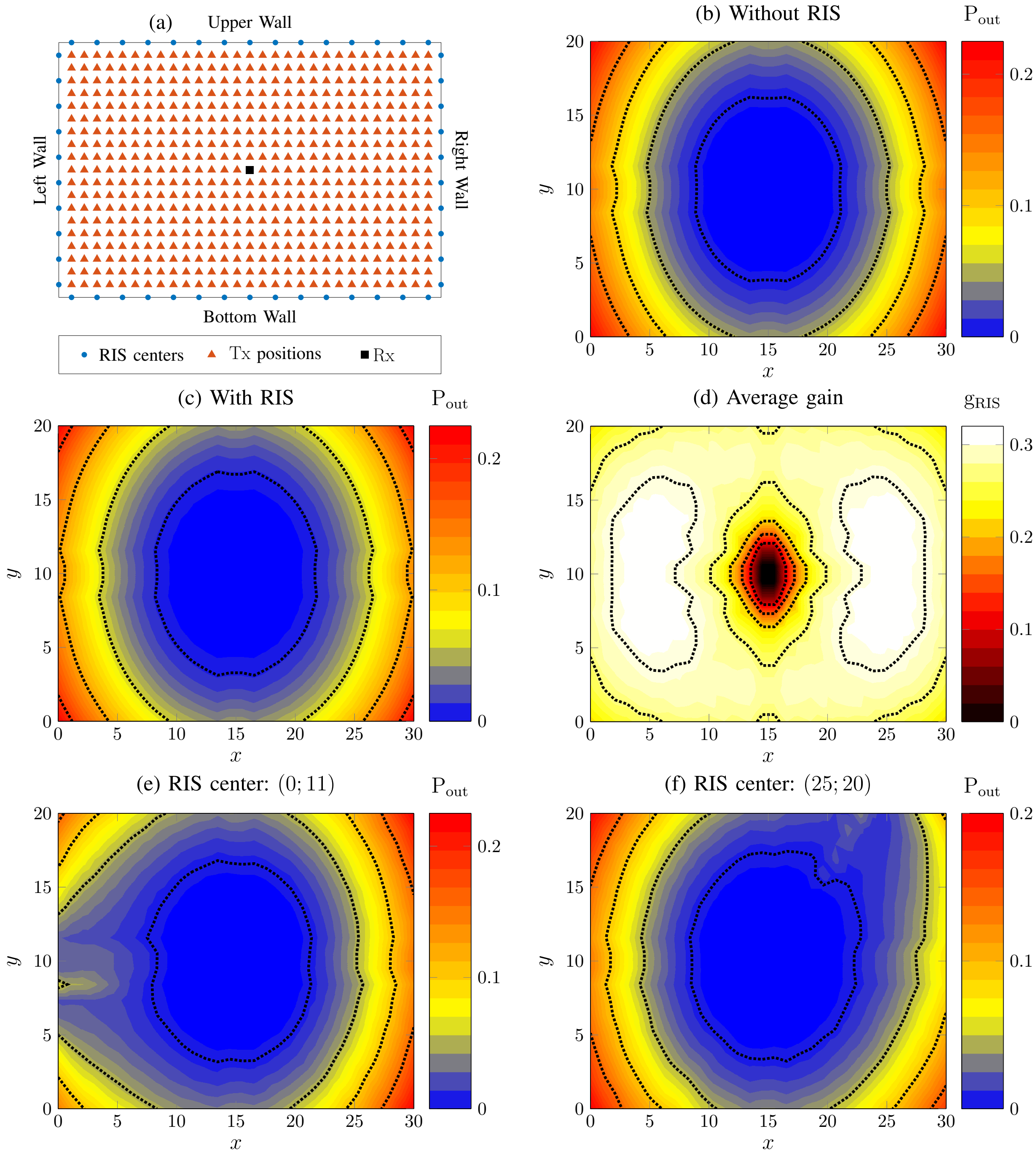

Fig. 3. (a) Simulated room geometry: The black square in the center represents the Rx, red triangles indicate tested Tx positions, and blue circles mark tested RIS positions. Outage probability versus Tx position at $\gamma_{th} = -10$ dB, $f = 18$ GHz, and $N = 128$: (b) Without RIS, (c) With RIS, (d) Average relative gain g_{RIS} attributed to the RIS, (e) With a RIS positioned at $(11, 0)$, and (f) With a RIS positioned at $(25, 20)$.

depict heatmaps illustrating the outage probability of the RIS-assisted wireless communication system across all Tx positions. These heatmaps correspond to two distinct positions of the RIS center, $(11, 0)$ and $(25, 20)$, respectively. It can be observed that the performance of the wireless systems in terms of outage probability significantly improves in the area surrounding the RIS.

B. Beam steering cases

In this section, we examine the performance of the RIS-assisted communication systems under various beam steering scenarios. In this regard, we first assess the quality of the RIS path relative to the LOS path in the absence of beam steering. Under this scenario, we can also observe the behavior of the RIS-assisted system when the LOS path is entirely blocked. For this purpose, Fig. 4(a) displays the outage probabilities versus the SNR threshold γ_{th} for the sole direct LOS path and the system utilizing only the RIS path across different numbers of RIS elements. These curves are obtained using an operating frequency of 18 GHz. In this case, we use the same positioning for the transmitter, receiver, and RIS center as in the indoor 2D case, i.e., (8,3), (15,10), and (12,0), respectively. Furthermore, we set $r = 10$ cm, $\lambda_{obs} = 0.5$ m^{-2}, $\mu_0 = 1$. $G_t = 20$ dB, $G_r = 10$ dB, $P_t = 0.1$ W, and $\sigma^2 = 1.65 \times 10^{-11}$ W. As illustrated in Fig. 4(a), without beam steering, the transmitter can establish a communication link with the receiver using only the RIS path. The link performance improves as the number of RIS

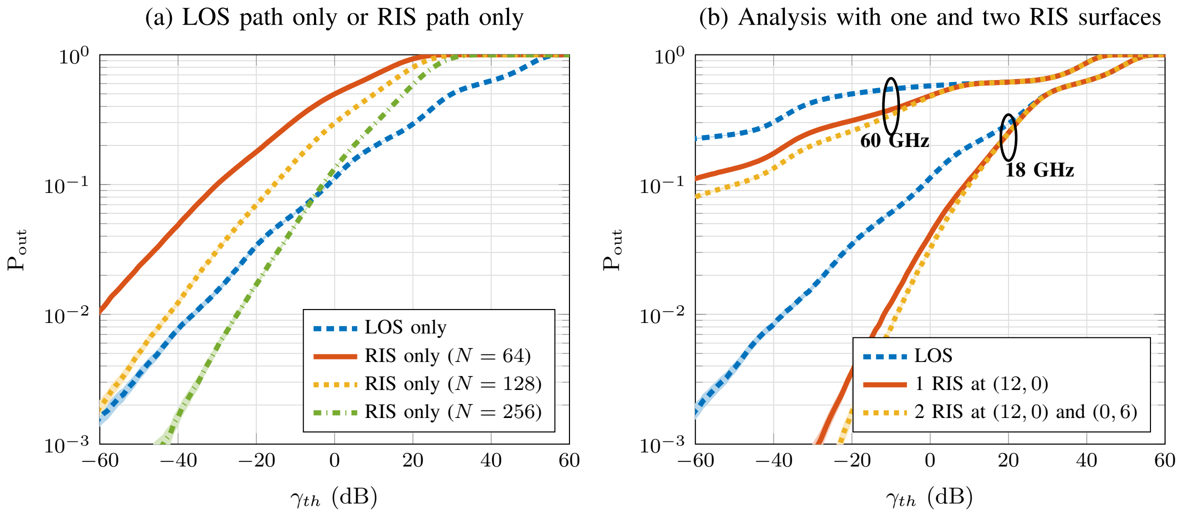

Fig. 4. Beam steering cases. (a) Outage probability (P_{out}) with 95% confidence interval as a function of SNR threshold (γ_{th}) for the direct LOS path only (LOS only) and the system considering only the RIS path (RIS only) using different numbers of RIS elements N (No beam steering) at an operating frequency of 18 GHz; (b) Outage probability with 95% confidence interval versus γ_{th} for the LOS path, a system aided by a single RIS with $N = 128$ elements positioned at coordinates $(12, 0)$ $(12, 0)$, and a system utilizing two RIS surfaces, each with $N = 128$ elements, centered at $(12, 0)$ and $(0, 6)$.

elements increases. In particular, the RIS path with $N = 128$ elements exhibits a similar SNR threshold to the LOS path for a probability of outage of $P_{out} = 0.001$, and the RIS path with $N = 256$ provides a gain of approximately 20 dB. Additionally, when SNR values range from 0 dB to 60 dB, the LOS path exhibits the best performance in terms of outage probability.

Furthermore, we investigate the performance of RIS-assisted systems under a beam steering scenario employing multiple RIS surfaces. In this context, Fig. 4(b) shows the outage probability as a function of the SNR threshold γ_{th} for three scenarios: the LOS path, a wireless communication system supported by a single RIS surface with $N = 128$ elements installed on the bottom wall centered at $(12, 0)$, and a system assisted by two RIS surfaces, each surface with $N = 128$ elements, mounted on the bottom and left walls at coordinates $(12, 0)$ and $(0, 6)$, respectively. The plotted curves correspond to two operating frequencies: 18 GHz and 60 GHz. Notice that beam steering using strongly directional antennas can establish the communication link between the transmitter and the receiver using any path. In the case of two RIS surfaces, the simulation computes three path losses: the LOS path loss, the path loss attributed to the RIS surface positioned at $(12, 0)$, and the path loss attributed to the second RIS surface centered at $(0, 6)$. Subsequently, the system selects the path with the least attenuation, as described in (20). As can be seen in Fig. 4(b), the inclusion of the second RIS exhibits a diminishing return effect since the second RIS improves the wireless link outage probability, but the improvement is significantly lower than the one achieved with the first RIS. Nevertheless, the availability of the second RIS yields a gain of approximately 5 dB for $P_{out} = 0.001$ at the operating frequency of 18 GHz. Outage probabilities at 60 GHz are larger than those obtained at 18 GHz. However, including one or two RISs yields remarkable SNR gains at 60 GHz for a given outage probability level compared to those achieved at 18 GHz.

C. Indoor 3D

Eventually, we present simulation results for a generic indoor 3D environment, which is the 3D extension of the

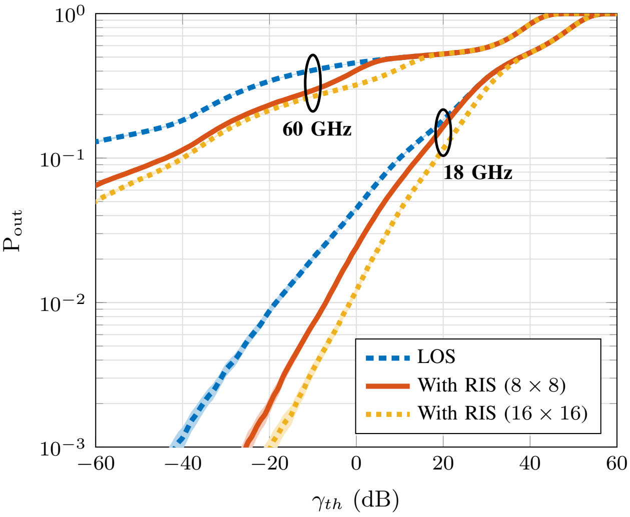

Fig. 5. Outage probability (P_{out}) with 95% confidence interval versus the SNR threshold (γ_{th}) for the direct LOS path (LOS) and the system considering the LOS and RIS paths (With RIS) using different numbers of RIS elements. Simulated indoor 3D environment: positions $\mathrm{Tx} : (8, 3, 1)$, $\mathrm{Rx} : (15, 10, 2.5)$, and RIS center at $(12, 0, 1.5)$.

2D environment considered so far. Moreover, we now take both $N > 1$ and $M > 1$ so that the RIS is a planar 2D surface with $N \times M$ cells of area $\delta_x \times \delta_z$. Obstructions are simulated as spheres of radius r.

Here, our simulations are confined to a parallelepipedal room measuring 20 meters in width, 30 meters in length, and 3 meters in height. These dimensions align with typical real-world 3D indoor settings in classrooms, conference rooms, and office spaces. Objects and humans can obstruct the wireless communication links in this 3D space within the room. More precisely, the mmWave transmitter is situated at coordinates $(8, 3, 1)$, while the receiver is located at $(15, 10, 2.5)$. We are considering the scenario where user equipment connects to the access point at the center of the room near the ceiling. In addition, the RIS is mounted on the x-z plane whose geometric center is placed at coordinates $(12, 0, 1.5)$. In the indoor 3D environment, we have set $\delta_x = \delta_z = \frac{\lambda}{2}$, $r = 10$ cm, $\lambda_{obs} = 2.00\ \mathrm{m}^{-3}$. In these simulations, we use

$\mu_0 = 1$. $G_t = 20$ dB, $G_r = 10$ dB, $P_t = 0.1$ W, and $\sigma^2 = 1.65 \times 10^{-11}$ W.

Figure 5 depicts the outage probability P_{out} against the SNR threshold γ_{th} for the indoor 3D scenario, showcasing two different array sizes of the RIS: 8×8 (equivalent to $N = 8$ and $M = 8$) and 16×16 (equivalent to $N = 16$ and $M = 16$). Outage probability curves are obtained for two operating frequencies: 18 GHz and 60 GHz. Consistent with observations in the 2D scenario, integrating a RIS markedly enhances communication link performance in terms of outage probability compared to relying solely on the LOS path. The gain offered by the RIS is of the order of several dB units concerning the SNR threshold γ_{th} at both tested frequencies. In particular, to achieve an outage probability of 0.1% ($\mathrm{P_{out}} = 0.001$) at 18 GHz, the improvements of the RIS-aided wireless system over the LOS path are approximately 17 dB and 20 dB for RIS arrays of 8×8 and 16×16 cells, respectively. The mere presence of a few cells brings most of the gain, while extending the RIS size further has a less impressive incremental impact. This is because in wider RIS, outer cells contribute less to reflection towards the receiver because they see the transmitter signal significantly off the peak according to the radiation pattern of its antenna. Moreover, with wide RIS structures, the total path length from Tx to Rx through a cell reflection can be substantially different from the center and outer RIS cells, with longer paths (passing by outer cells) having a higher probability of intercepting more obstructions. Therefore, the incremental gain due to adding extra cells fades off quickly.

IV. Conclusion

This paper presents a comprehensive path loss model for wireless communication systems assisted by reconfigurable intelligent surfaces (RISs). This model accounts for the compounded impact of the attenuation of the transmission medium and obstacles obstructing link paths. It should be noted that estimating the obstruction length caused by objects along both the path from the transmitter to a RIS element and the path from a RIS element to the receiver is essential for accurately determining the RIS path losses.

We applied the path loss model to assess the outage probability of RIS-assisted systems within indoor settings, considering randomly positioned obstacles. Our evaluation of RIS-aided communication systems focused on outage probability across various parameters, such as the number of RIS elements, signal-to-noise ratio (SNR), obstruction density, and width of obstruction objects.

Moreover, we examined the impact of different RIS positions and transmitter locations on outage probability. In this sense, we quantified the average relative gain achieved by integrating a RIS surface within an indoor environment. We also evaluated the performance of RIS-assisted systems in different beam steering scenarios. Furthermore, we include the results of RIS-assisted wireless systems for indoor 2D and 3D cases. Our results show that significant benefits can be obtained by adding a RIS to the communication system.

In the future, we intend to develop a simple model of the path loss distribution for the RIS path in the near field, based on stochastic geometry. The model will enable us to calculate the outage probability analytically.

References

[1] Faisal Tariq, Muhammad R. A. Khandaker, Kai-Kit Wong, Muhammad A. Imran, Mehdi Bennis, and Merouane Debbah, "A Speculative Study on 6G," *IEEE Wireless Communications*, vol. 27, no. 4, pp. 118–125, 2020.

[2] Ozan Alp Topal, Mustafa Ozger, Dominic Schupke, Emil Björnson, and Cicek Cavdar, "mmWave Communications for Indoor Dense Spaces: Ray-Tracing Based Channel Characterization and Performance Comparison," in *ICC 2022 - IEEE International Conference on Communications*, 2022, pp. 516–521.

[3] Chongwen Huang, Alessio Zappone, George Alexandropoulos, Mérouane Debbah, and Chau Yuen, "Reconfigurable Intelligent Surfaces for Energy Efficiency in Wireless Communication," *IEEE Transactions on Wireless Communications*, vol. 18, no. 8, pp. 4157–4170, 2019.

[4] Marco Di Renzo, Alessio Zappone, Merouane Debbah, Mohamed-Slim Alouini, Chau Yuen, Julien de Rosny, and Sergei Tretyakov, "Smart Radio Environments Empowered by Reconfigurable Intelligent Surfaces: How It Works, State of Research, and The Road Ahead," *IEEE Journal on Selected Areas in Communications*, vol. 38, no. 11, pp. 2450–2525, 2020.

[5] Steven W. Ellingson, "Path Loss in Reconfigurable Intelligent Surface-Enabled Channels," in *2021 IEEE 32nd Annual International Symposium on Personal, Indoor and Mobile Radio Communications (PIMRC)*, 2021, pp. 829–835.

[6] Wankai Tang, Ming Zheng Chen, Xiangyu Chen, Jun Yan Dai, Yu Han, Marco Di Renzo, Yong Zeng, Shi Jin, Qiang Cheng, and Tie Jun Cui, "Wireless Communications With Reconfigurable Intelligent Surface: Path Loss Modeling and Experimental Measurement," *IEEE Transactions on Wireless Communications*, vol. 20, no. 1, pp. 421–439, 2021.

[7] Wankai Tang, Xiangyu Chen, Ming Zheng Chen, Jun Yan Dai, Yu Han, Marco Di Renzo, Shi Jin, Qiang Cheng, and Tie Jun Cui, "Path Loss Modeling and Measurements for Reconfigurable Intelligent Surfaces in the Millimeter-Wave Frequency Band," *IEEE Transactions on Communications*, vol. 70, no. 9, pp. 6259–6276, 2022.

[8] Marco Di Renzo, Fadil Habibi Danufane, Xiaojun Xi, Julien de Rosny, and Sergei Tretyakov, "Analytical Modeling of the Path-Loss for Reconfigurable Intelligent Surfaces – Anomalous Mirror or Scatterer?," in *2020 IEEE 21st International Workshop on Signal Processing Advances in Wireless Communications (SPAWC)*, 2020, pp. 1–5.

[9] Gabriele Gradoni and Marco Di Renzo, "End-to-End Mutual Coupling Aware Communication Model for Reconfigurable Intelligent Surfaces: An Electromagnetic-Compliant Approach Based on Mutual Impedances," *IEEE Wireless Communications Letters*, vol. 10, no. 5, pp. 938–942, 2021.

[10] Marzieh Najafi, Vahid Jamali, Robert Schober, and H. Vincent Poor, "Physics-Based Modeling and Scalable Optimization of Large Intelligent Reflecting Surfaces," *IEEE Transactions on Communications*, vol. 69, no. 4, pp. 2673–2691, 2021.

[11] Jie Huang, Cheng-Xiang Wang, Yingzhuo Sun, Rui Feng, Jialing Huang, Bolun Guo, Zhimeng Zhong, and Tie Jun Cui, "Reconfigurable Intelligent Surfaces: Channel Characterization and Modeling," *Proceedings of the IEEE*, vol. 110, no. 9, pp. 1290–1311, 2022.

[12] Amr A. Abdelnabi, Vincenzo Mancuso, and Marco Ajmone Marsan, "Outage of Millimeter Wave Links With Randomly Located Obstructions," *IEEE Access*, vol. 8, pp. 139404–139421, 2020.

[13] Richard Weiler, Michael Peter, Wilhelm Keusgen, Alexander Maltsev, Ingolf Karls, Andrey Pudeyev, Ilya Bolotin, Isabelle Siaud, and Anne-Marie Ulmer-Moll, "Quasi-deterministic millimeter-wave channel models in MiWEBA," *EURASIP Journal on Wireless Communications and Networking*, vol. 2016, pp. 1–16, 2016.

[14] Leonardo Badia, Vincenzo Mancuso, and Marco Ajmone Marsan, "Adversarial Obstruction of Millimeter Wave Links," in *2023 21st Mediterranean Communication and Computer Networking Conference (MedComNet)*, 2023, pp. 101–110.

[15] Zhenyu Li, Ozan Alp Topal, Özlem Tuğfe Demir, Emil Björnson, and Cicek Cavdar, "mmWave Coverage Extension Using Reconfigurable Intelligent Surfaces in Indoor Dense Spaces," in *ICC 2023 - IEEE International Conference on Communications*, 2023, pp. 5805–5810.

[16] Ahmed Al-Saman, Michael Cheffena, Olakunle Elijah, Yousef A Al-Gumaei, Sharul Kamal Abdul Rahim, and Tawfik Al-Hadhrami, "Survey of millimeter-wave propagation measurements and models in indoor environments," *Electronics*, vol. 10, no. 14, pp. 1653, 2021.